SUBMITTED MANUSCRIPT

Efficient Fully Bayesian Approach to Brain Activity Mapping with Complex-Valued fMRI Data

Zhengxin Wang[a], Daniel B. Rowe[b], Xinyi Li[a] and D. Andrew Brown[a]

[a]School of Mathematical and Statistical Sciences, Clemson University, Clemson, SC, USA; [b]Department of Mathematical and Statistical Sciences, Marquette University, Milwaukee, WI, USA

ARTICLE HISTORY
Compiled June 28, 2024

ABSTRACT
Functional magnetic resonance imaging (fMRI) enables indirect detection of brain activity changes via the blood-oxygen-level-dependent (BOLD) signal. Conventional analysis methods mainly rely on the real-valued magnitude of these signals. In contrast, research suggests that analyzing both real and imaginary components of the complex-valued fMRI (cv-fMRI) signal provides a more holistic approach that can increase power to detect neuronal activation. We propose a fully Bayesian model for brain activity mapping with cv-fMRI data. Our model accommodates temporal and spatial dynamics. Additionally, we propose a computationally efficient sampling algorithm, which enhances processing speed through image partitioning. Our approach is shown to be computationally efficient via image partitioning and parallel computation while being competitive with state-of-the-art methods. We support these claims with both simulated numerical studies and an application to real cv-fMRI data obtained from a finger-tapping experiment.

KEYWORDS
Gibbs sampling; parallel computation, spike and slab prior, variable selection

1. Introduction

Functional magnetic resonance imaging (fMRI) is a non-invasive brain imaging technique that records signals generated by changes in blood oxygenation levels associated with neuronal activity. This so-called blood-oxygenation-level-dependent (BOLD) signal thus facilitates indirect monitoring of brain activity over time [3]. During task-based fMRI experiments, subjects experience intermittent stimuli, such as viewing images or finger tapping. As the brain responds to a particular stimulus, neuronal activity in certain regions intensifies, leading to increased oxygen consumption. This metabolic change subsequently increases the BOLD response in that region. These BOLD fluctuations impact local magnetic susceptibility, thereby affecting the resulting fMRI signal [19]. Empirical studies have demonstrated that the expected BOLD response in an activated brain region, in reaction to binary "boxcar" stimuli (repeated identical on-off periods), can be accurately modeled by convolving the boxcar 0-1 stimulus variable with a gamma or double-gamma hemodynamic response function (HRF) [6, 20].

CONTACT D. Andrew Brown. Email: ab7@clemson.edu

Signals generated by magnetic resonance imaging machines are complex-valued with both real and imaginary components due to forward and inverse Fourier transformations that occur in the presence of phase imperfections [7]. However, most fMRI studies for brain activity mapping only analyze the magnitudes of the MR signals, as the phase components are typically discarded as part of preprocessing. To identify active voxels in response to a stimulus, a linear model is commonly used [12, 19]. Specifically, any voxel (volumetric pixel) whose BOLD signal magnitude significantly changes over time in response to the stimulus will be considered an active voxel. The magnitude-only approach carries several limitations. For one, the magnitude-only models typically operate on the assumption of normally distributed errors. However, even when the original real and imaginary components of the data possess such Gaussian errors, the magnitude follows a Ricean distribution that is approximately normal only for large signal-to-noise ratios (SNRs) [14, 30]. Large SNRs are not always present, making the Gaussian assumption less tenable, thereby losing power. Moreover, by discarding phase information, we ignore half of the available data that may contain information about the underlying neurophysiological processes. On the other hand, using complex-valued fMRI (cv-fMRI) data for analysis has shown promising results. By fully incorporating both real and imaginary components, cv-fMRI studies allow for more comprehensive and accurate models with greater power to detect task-related neuronal activity. Such models often handle SNR more appropriately and make full use of the data at hand, thereby yielding potentially more informative insights into brain activity [1, 18, 31–33, 35–37, 43].

To determine task-related brain activation maps from fMRI signals, fully Bayesian approaches stand out due to their ability to flexibly model spatial and temporal correlations. In this paper, we propose a fully Bayesian model for brain activity mapping using single-subject cv-fMRI time series. Specifically, we aim to determine which voxels' fMRI signal magnitudes (assuming constant phase) change significantly in response to a particular task, as well as the amount of the change. An effective Bayesian approach for fMRI data analysis should fully utilize both the real and imaginary parts of the fMRI data, capture spatiotemporal correlations, provide high prediction accuracy, and be computationally efficient. Although previous studies have made progress in some of these areas [4, 23, 39, 42, 44], no single model has yet achieved all of these goals. Our proposed approach uses autoregressive models for the temporal correlations and Gaussian Markov random fields [GMRFs; 38] to capture spatial associations in the cv-fMRI data. Moreover, we employ image partitioning and parallel computation to facilitate computationally efficient Markov chain Monte Carlo [MCMC; 13] algorithms.

The remainder of the paper is organized as follows. Section 2 details our proposed model, outlines the priors and posteriors, and explains our strategy for brain partitioning. We demonstrate estimation and inference in Section 3, where we use simulated datasets to test the performance of our model in terms of the determination of brain activity maps. Section 4 shows the results of implementing our proposed approach on cv-fMRI data obtained from real finger-tapping experiment. Lastly, Section 5 summarizes our findings, highlights our contributions, and outlines potential work for future research in this domain.

2. Model

In this section, we present our model for brain activity mapping with cv-fMRI data, including an equivalent real-valued representation. We also describe the brain parcel-

lation strategy for parallel computation. We derive the posterior distribution of the parameters of interest, as well as an MCMC algorithm for accessing it.

2.1. Model formulation

FMRI, both real- and complex-valued, are known to exhibit temporal correlations. This can be captured by autoregressive (AR) error structure. Thus, our complex-valued model is based on that proposed by [18], with some modifications. For the v^{th} voxel, $v = 1, ..., V$, the measured signal is modeled as

$$\mathbf{y}^v = \mathbf{x}\beta^v + \mathbf{r}^v\rho^v + \boldsymbol{\varepsilon}^v, \tag{1}$$

where all terms are complex-valued except $\mathbf{x}$. The term $\mathbf{y}^v \in \mathbb{C}^T$ is the vector of signals at voxel v collected at evenly-spaced time points, where T is the total observed time points. The term $\mathbf{x} \in \mathbb{R}^T$ denotes the vector of the expected BOLD response, which is obtained by convolving the boxcar stimulus, such as finger tapping, image viewing, or similar "on/off" conditions, with a double-gamma HRF associated with a particular stimulus. The regression coefficient is denoted by $\beta^v \in \mathbb{C}$. We assume that low-frequency trends in $\mathbf{y}^v$ have been removed by preprocessing, and that both $\mathbf{y}^v$ and $\mathbf{x}$ are centered. The term $\mathbf{r}^v \in \mathbb{C}^T$ is the vector of lag-1 prediction errors for the assumed AR(1) model, with $\rho^v \in \mathbb{C}$ the scalar autoregression coefficient. Temporally-correlated errors are typically present in fMRI signals [17, 26], and the AR(1) model has been demonstrated to be sufficient for capturing temporal dynamics in fMRI data [8]. We suppose that the error term $\boldsymbol{\varepsilon}^v$ follows the standard complex normal distribution; that is, $\boldsymbol{\varepsilon}^v \sim \mathcal{CN}_T(\boldsymbol{\mu}^v = \mathbf{0}, \boldsymbol{\Gamma}^v = 2\sigma_v^2\mathbf{I}, \mathbf{C}^v = \mathbf{0})$, where $\mathcal{CN}_T$ denotes a complex normal distribution of dimension T with mean $\boldsymbol{\mu}^v$, complex-valued, Hermitian and non-negative definite covariance matrix $\boldsymbol{\Gamma}^v$, and complex-valued symmetric relation matrix $\mathbf{C}^v$. In the appendix, we provide details similar to those presented by [33] that demonstrate the equivalence between the model of [18] and the cv-fMRI model proposed by [35] with constant phase.

[25] and [43] provide an equivalent real-valued representation of model (1) as

$$\underbrace{\begin{pmatrix}\mathbf{y}^v_{Re}\\ \mathbf{y}^v_{Im}\end{pmatrix}}_{\mathbf{y}^v_r} = \underbrace{\begin{pmatrix}\mathbf{x} & \mathbf{0}\\ \mathbf{0} & \mathbf{x}\end{pmatrix}}_{\mathbf{X}_r}\underbrace{\begin{pmatrix}\beta^v_{Re}\\ \beta^v_{Im}\end{pmatrix}}_{\boldsymbol{\beta}^v_r} + \underbrace{\begin{pmatrix}\mathbf{r}^v_{Re} & -\mathbf{r}^v_{Im}\\ \mathbf{r}^v_{Im} & \mathbf{r}^v_{Re}\end{pmatrix}}_{\mathbf{R}^v_r}\underbrace{\begin{pmatrix}\rho^v_{Re}\\ \rho^v_{Im}\end{pmatrix}}_{\boldsymbol{\rho}^v_r} + \underbrace{\begin{pmatrix}\boldsymbol{\varepsilon}^v_{Re}\\ \boldsymbol{\varepsilon}^v_{Im}\end{pmatrix}}_{\boldsymbol{\varepsilon}^v_r},$$

where all terms are real-valued. Using the symbols in the underbraces, this is more concisely written as

$$\mathbf{y}^v_r = \mathbf{X}_r\boldsymbol{\beta}^v_r + \mathbf{R}^v_r\boldsymbol{\rho}^v_r + \boldsymbol{\varepsilon}^v_r, \qquad \boldsymbol{\varepsilon}^v_r \sim \mathcal{N}_{2T}(\mathbf{0}, \boldsymbol{\Sigma}^v),$$

where

$$\boldsymbol{\Sigma}^v = \begin{pmatrix}\boldsymbol{\Sigma}^v_{Re,Re} & \boldsymbol{\Sigma}^v_{Re,Im}\\ \boldsymbol{\Sigma}^v_{Im,Re} & \boldsymbol{\Sigma}^v_{Im,Im}\end{pmatrix},$$

and

$$\begin{aligned}\boldsymbol{\Sigma}^v_{Re,Re} &= \tfrac{1}{2}Re(\boldsymbol{\Gamma}^v + \mathbf{C}^v) = \sigma_v^2\mathbf{I}_T, \quad & \boldsymbol{\Sigma}^v_{Re,Im} &= \tfrac{1}{2}Im(-\boldsymbol{\Gamma}^v + \mathbf{C}^v) = \mathbf{0}_T,\\ \boldsymbol{\Sigma}^v_{Im,Re} &= \tfrac{1}{2}Im(\boldsymbol{\Gamma}^v + \mathbf{C}^v) = \mathbf{0}_T, \quad & \boldsymbol{\Sigma}^v_{Im,Im} &= \tfrac{1}{2}Re(\boldsymbol{\Gamma}^v - \mathbf{C}^v) = \sigma_v^2\mathbf{I}_T.\end{aligned}$$

Observe that our assumption on the covariance structure here simply means that $\mathbf{\Sigma}^v = \sigma_v^2 \mathbf{I}_{2T}$. We assign the voxel- specific variances σ_v^2 and autoregression coefficient $\boldsymbol{\rho}_r^v$ Jeffreys prior and uniform prior, respectively. That is, $p(\sigma_v^2) = 1/\sigma_v^2$ and $p(\boldsymbol{\rho}_r^v) = 1$, for $v = 1, \ldots, V$.

2.2. Brain parcellation and spatial priors

In addition to temporal dependence, fMRI signals also exhibit spatial associations. These spatial dependencies can originate from several sources, including the inherent noise of the data [16], unmodeled neuronal activation [5], and preprocessing steps such as spatial normalization [11], image reconstruction [34], and spatial smoothing [21]. Hence voxels, as artificial partitions of the human brain, often exhibit behavior similar to that of their neighbors. These spatial dependencies can be modeled by imposing spatial structure in the prior on β^v or the hyperparameters in such priors.

Brain parcellation [23] propose a brain parcellation technique that seeks to identify active voxels within each parcel/partition, and subsequently combines these results to generate a comprehensive whole-brain activity map. The authors partition their brain images into initial parcels of size approximately 500 voxels each. If a parcel is found to be too large or too small, it is broken down into voxels and these voxels are merged into adjacent parcels while ensuring the merged parcels contain less than 1000 voxels each. Alternatively, the partitioning strategy could be based on anatomical atlases such as Brodmann areas [2, 40], or based on equal geometric size in the image rather than equal numbers of contained voxels. [23] remark that this method of partitioning induces negligible edge effects; that is, the classification of voxels on the borders of parcels is not strongly affected.

In our study, we partition the two- or three-dimensional fMRI image into G parcels of approximately equal geometric size. We then process each parcel independently using the same model and method, facilitating parallel computation and hence computational efficiency. We find that our parcellation strategy incurs minimal edge effects, echoing the observations of [23]. We discuss the optimal number of parcels and corresponding number of voxels in each parcel in the appendix.

Prior distribution of $\boldsymbol{\beta^v}$ For parcel g, $g = 1, \ldots, G$, containing V_g voxels, a voxel v ($v = 1, \ldots, V_g$) is classified as an active voxel under the stimulus if its regression coefficient of slope $\beta^v = \beta_{Re}^v + i\beta_{Im}^v \neq 0$, where i is the imaginary unit. As this is a variable selection problem, we use a spike-and-slab prior [22, 43]:

$$\beta^v \mid \gamma_v \sim \gamma_v \mathcal{CN}_1(0, 2\tau_g^2, 0) + (1 - \gamma_v)\mathcal{I}_0, \tag{2}$$

where $\mathcal{I}_0$ denotes the point mass at 0. The binary indicator $\gamma_v \in \{0, 1\}$ reflects the status of a voxel. Specifically, $\gamma_v = 1$ indicates that voxel v is responding to the task, while $\gamma_v = 0$ otherwise. We take $\tau_g^2 \in \mathbb{R}$ to be constant across all voxels within each parcel. [43] shows that a real-valued representation of (2) is given by:

$$\boldsymbol{\beta}_r^v = \begin{pmatrix} \beta_{Re}^v \\ \beta_{Im}^v \end{pmatrix} \mid \gamma_v \sim \mathcal{N}_2(\mathbf{0},\ \gamma_v \tau_g^2 \mathbf{I}).$$

The parcel specific variances τ_g^2 are assigned a Jeffreys prior, $p(\tau_g^2) = 1/\tau_g^2$, $g = 1, \ldots, G$.

Spatial prior on $\boldsymbol{\gamma_v}$ To further reduce computational effort and to capture pertinent spatial structure with a low-dimensional representation, we employ the sparse spatial generalized linear mixed model (sSGLMM) prior, as developed by [15] and [23], which is in turn an extension of the the prior proposed by [29]. Such priors use GMRFs and reduce the dimension by examining the spectra of the associated Markov graphs. For voxel v ($v = 1, ..., V_g$) within parcel g ($g = 1, ..., G$), we suppose that

$$\begin{aligned} \gamma_v \mid \eta_v &\overset{iid}{\sim} \mathcal{B}ern\left\{\boldsymbol{\Phi}(\psi + \eta_v)\right\}, \\ \eta_v \mid \boldsymbol{\delta}_g &\sim \mathcal{N}_1\left(\mathbf{m}_v'\boldsymbol{\delta}_g, 1\right), \\ \boldsymbol{\delta}_g \mid \kappa_g &\sim \mathcal{N}_q\left\{\mathbf{0}, (\kappa_g \mathbf{M}_g{}'\mathbf{Q}_g\mathbf{M}_g)^{-1}\right\}, \\ \kappa_g &\sim \mathcal{G}amma\left(a_\kappa, b_\kappa\right), \end{aligned} \tag{3}$$

where $\boldsymbol{\Phi}(\cdot)$ denotes the CDF of the standard normal distribution and $\psi \in \mathbb{R}$ is a fixed tuning parameter. The terms $\mathbf{m}_v'$, $\mathbf{M}_g$, and $\mathbf{Q}_g$ are derived from the adjacency matrix $\mathbf{A}_g$ of parcel g. The adjacency matrix $\mathbf{A}_g \in \{0,1\}^{V_g \times V_g}$ is such that $\mathbf{A}_{g,uv} = 1$ if voxels u and v are neighbors in the image, and 0 otherwise, where "neighbor" is defined by the user. Typically, voxels that share an edge or a corner are taken to be neighbors. The matrix $\mathbf{M}_g \in \mathbb{R}^{V_g \times q}$ contains the first q principal eigenvectors of $\mathbf{A}_g$, typically with $q \ll V_g$. The term $\mathbf{m}_v'$ is a $1 \times q$ row vector of "synthetic spatial predictors" [15] corresponding to the v^{th} row of $\mathbf{M}_g$. The matrix $\mathbf{Q}_g = \text{diag}(\mathbf{A}_g\mathbf{1}_{V_g}) - \mathbf{A}_g$ is the graph Laplacian. The term $\boldsymbol{\delta}_g$ is a $q \times 1$ vector of spatial random effects, and κ_g is the spatial smoothing parameter.

The design of the prior distribution for binary indicator γ_v aims to capture both spatial dependencies and the sparsity of active voxels. This reflects the hypothesis that a voxel is more likely to be active/inactive if their neighboring voxels are also active/inactive [12, 39]. Furthermore, in the context of simple tasks, only a small percentage of voxels across the entire brain are expected to be active [9, 28]. Thus the sSGLMM prior is well-suited to the work and compatible with the parcellation approach. [15] remark that $\mathbf{M}_g$ is capable of capturing smooth patterns of spatial variation at various scales.

The parameters ψ, q, a_κ, and b_κ are fixed *a priori* and determined based on several factors. In our simulation studies, we examine various values of ψ, and the one provides the highest prediction accuracy is used to present the results. The effect of different ψ values is evaluated in the Supplementary Material. For real human datasets, the initial value of ψ is set to $\boldsymbol{\Phi}^{-1}(0.02) = -2.05$ for all voxels, following the suggestion of [23]. This value can be further adjusted based on the proportion of active voxels detected in previous experiments. We set $q = 5$ (when V_g is approximately 200) per [15], indicating that such a reduction is often feasible. We find there is no detectable difference using larger q. The shape and scale parameters of the gamma distribution, $a_\kappa = \frac{1}{2}$ and $b_\kappa = 2000$ respectively, are selected to yield a large mean for κ_g ($a_\kappa b_\kappa$=1000). This choice serves to reduce the chances of creating misleading spatial structures in the posterior distribution, mitigating the risk of identifying spurious brain activity patterns that could be attributed to noise or other confounding factors.

2.3. MCMC algorithm and posterior distributions

We use Gibbs sampling to obtain the joint and marginal posterior distributions of parameters of interest. The necessary full conditional distributions and derivations are outlined in the appendix. The fixed-width approach proposed by [10] is used to diagnose convergence. Specifically, we consider the algorithm to have converged if the Monte Carlo standard error (MCSE) of any γ_v is less than 0.05. In our numerical studies that follow, we run 10^3 iterations. We take the means of the sampled parameters (after discarding burn-in iterations) as the point estimates. Active voxels are determined by $\widehat{\gamma}_v > 0.8722$ [39], and $\widehat{\beta}^v_{Re}$ and $\widehat{\beta}^v_{Im}$ are used to construct the estimated magnitude maps, computed as $\sqrt{(\widehat{\beta}^v_{Re})^2 + (\widehat{\beta}^v_{Im})^2}$.

3. Simulation studies

In this section, we simulate two types of two-dimensional complex-valued time series of fMRI signals: data with *iid* noise and data with noise following AR(1) temporal dependence. We evaluate three models based on their performance in both classification and estimation fidelity. The models under consideration include:

- The model of [23], which uses a sSGLMM prior for magnitude-only data and incorporates brain parcellation (denoted as MO-sSGLMM).
- The model of [43] for cv-fMRI, which does not incorporate a spatial prior or brain parcellation (denoted as CV-nonSpatial). In this model, the prior for γ_v in model (3) is taken to be $\gamma_v \mid \eta_v \overset{iid}{\sim} \mathcal{B}ern(\eta_v), \eta_v \sim \mathcal{B}eta(1,1)$.
- Our proposed model, which uses an sSGLMM prior for complex-valued data and incorporates brain parcellation (denoted as CV-sSGLMM).

All three models are fully Bayesian, suitable for autoregressive noise, and leverage Gibbs sampling to approximate their respective posterior distributions. Both MO-sSGLMM and CV-sSGLMM use the best combination of parcel number G and tuning parameter ψ in terms of the prediction accuracy ($G = 9$ and $\psi = \Phi^{-1}(0.47)$ for both), and determine the active voxels by thresholding at $\widehat{\gamma}_v > 0.8722$. The impacts of the tuning parameter ψ and the number of parcels G are provided in the appendix. The CV-nonSpatial model uses a threshold of 0.5, as suggested by [43].

All of the results are generated by running the code on a custom-built desktop computer with an Intel Core i9-9980XE CPU (3.00GHz, 3001 Mhz, 18 cores, 36 logical processors), NVIDIA GeForce RTX 2080 Ti GPU, 64 GB RAM, and operating on Windows 10 Pro.

3.1. Designed stimulus, expected BOLD response, and true activation/magnitude map

We use the same pattern of stimulus as simulated by [43]. The designed stimulus is a binary signal $\mathbf{s}$ consisting of five epochs, each with a duration of 40 time points, resulting in a total of $T = 200$ time points. Within each epoch, the stimulus is turned on and off for an equal duration of 20 time points. The expected BOLD response, denoted as $\mathbf{x}$, is generated by convolving the stimulus signal with a double-gamma HRF. Both the designed stimulus and expected BOLD response, depicted in Figures 1a and 1b, are shared for all simulated datasets.

maps.png

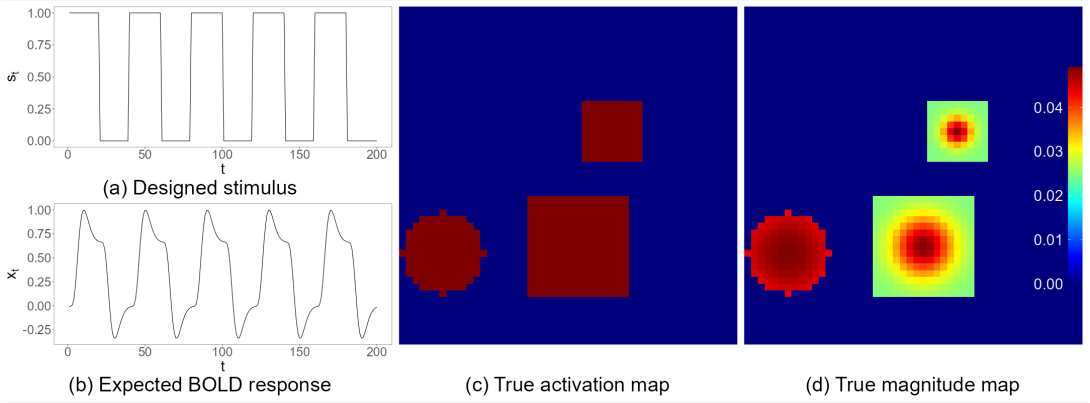

Figure 1. (a) Designed stimulus; (b) Expected BOLD response; (c) True activation map; (d) True magnitude map.

Table 1. Characteristics of true maps.

Map size	Number of active regions	Radius	Shape	Decay rate (ϱ)
50×50	3	2 to 6	sphere or cube	0 to 0.3

To simulate 100 replicates on a 50×50 panel, we use the `specifyregion` function in the `neuRosim` library [41] in `R` [27]. Each map features three non-overlapping active regions with varying characteristics such as centers, shapes, radii, and decay rates as shown in Table 1. The central voxel of an active region has a magnitude of one, while the magnitudes of the surrounding active voxels decrease based on their distance to the center and the decay rate ϱ. These magnitudes are further scaled by a multiplier of 0.04909 (which determines to the contrast-to-noise ratio via Eq. (4)), yielding a range of 0 to 0.04909. Examples of the true activation map and true magnitude map are shown in Figures 1c and 1d.

3.2. Simulating fMRI signals with non-AR noise and AR(1) noise

We simulate 100 datasets with *iid* noise using the expected BOLD response and each true magnitude map for CV-nonSpatial and CV-sSGLMM. We then extract the moduli to use with MO-sSGLMM. The cv-fMRI signal of voxel v at time t is simulated by:

$$\begin{aligned} y^v_{t,Re} &= (\beta_0 + \beta^v_1 x_t)\cos(\theta) + \varepsilon^v_{t,Re}, \quad \varepsilon^v_{t,Re} \sim \mathcal{N}(0, \sigma^2), \\ y^v_{t,Im} &= (\beta_0 + \beta^v_1 x_t)\sin(\theta) + \varepsilon^v_{t,Im}, \quad \varepsilon^v_{t,Im} \sim \mathcal{N}(0, \sigma^2), \end{aligned} \tag{4}$$

where x_t represents the expected BOLD response from Figure 1b at time t, and β^v_1 refers to the true magnitude of voxel v taken from Figure 1d. The phase, θ, is set to be the constant $\pi/4$, and σ is set to the constant 0.04909. As a result, the maximum contrast-to-noise ratio (CNR) is $\max \beta^v_1/\sigma = 1$. We determine the intercept β_0 based on the signal-to-noise ratio (SNR) such that SNR $= \beta_0/\sigma = 10$, leading to $\beta_0 = 0.4909$.

Next, we generate 100 datasets with AR(1) noise in a similar manner as Eq. (4).

The difference lies in the simulation of error terms, which is done so that

$$\begin{pmatrix} \varepsilon^v_{t,Re} \\ \varepsilon^v_{t,Im} \end{pmatrix} = \begin{pmatrix} 0.2 & -0.9 \\ 0.9 & 0.2 \end{pmatrix} \begin{pmatrix} \varepsilon^v_{t-1,Re} \\ \varepsilon^v_{t-1,Im} \end{pmatrix} + \begin{pmatrix} \xi^v_{Re} \\ \xi^v_{Im} \end{pmatrix}, \quad \begin{pmatrix} \xi^v_{Re} \\ \xi^v_{Im} \end{pmatrix} \sim \mathcal{N}_2\left(\mathbf{0}, \sigma^2\mathbf{I}\right).$$

This is a real-valued equivalent of the complex AR(1) error model,

$$\varepsilon^v_t = (0.2 + 0.9i)\varepsilon^v_{t-1} + \xi_v, \quad \xi_v \sim \mathcal{CN}_1(0, 2\sigma^2, 0). \tag{5}$$

3.3. Results

Results from our simulations are displayed in Figure 2, which depicts the estimated maps for a single dataset. The estimated activation maps are determined by $\widehat{\gamma}_v > 0.8722$, and the estimated magnitude maps are plotted by $\sqrt{(\widehat{\beta}^v_{Re})^2 + (\widehat{\beta}^v_{Im})^2}$, as explained in Section 2.3. The yellow grid lines correspond to the partitions in cases of brain parcellation. The performance across the three models reveals a consistent trend. All models perform well for the *iid* case, while MO-sSGLMM fails to detect any activity in the presence of the AR(1) noise. This is because the complex-valued AR structure in equation (5) cannot be recovered after extracting the moduli of the data. Further quantitative results, such as the receiver operating characteristic area under curve (ROC-AUC), true vs estimated magnitude regression slope, the concordance correlation coefficient (CCC), and true vs estimate pairwise mean square error (X-Y pairwise MSE), are illustrated in Figure 3. These offer a comprehensive performance evaluation in terms of classification and estimation. Figure 3 shows similar comparative performance as can be gleaned from Figure 2. All procedures do well in the presence of *iid* noise, whereas both complex-valued models considerably outperform the magnitude-only model when the errors are correlated. In each case, we can observe slightly better MSE, CCC, and estimation fidelity (Figure 3(b), (c), (d), (f), (g), (h)), but these are small when compared to the outperformance of the complex-valued models versus magnitude only.

Table 2 summarizes the average metrics across 100 *iid* noise and 100 AR(1) noise replicated datasets. In the *iid* case, the F1-score, slope, CCC, and X-Y MSE clearly favor MO-sSGLMM, followed by our CV-sSGLMM, and CV-nonSpatial ranks last. This demonstrates the proficiency of MO-sSGLMM on datasets where the necessity to capture complex-valued noise dependence is not crucial. The ROC-AUC score of MO-sSGLMM is comparable to that of CV-nonSpatial, and slightly surpasses that of our proposed CV-sSGLMM.

In the analysis of AR(1) datasets, our proposed CV-sSGLMM shows a clear advantage over the two competitors. Due to MO-sSGLMM's limitations already shown, we focus our comparison here between CV-nonSpatial and CV-sSGLMM. The CV-sSGLMM outperforms CV-nonSpatial across multiple metrics, such as F1-score, slope, CCC, and X-Y MSE. The superior performance of the CV-sSGLMM in terms of both classification and estimation can be attributed to the inclusion of the sSGLMM prior. In addition to our results, the value of using spatial priors to enhance the model's performance on correlated datasets has been demonstrated by [44]. Perhaps the most notable and favorable performance of our proposed model is in the vastly computational efficiency due to the brain parcellation and parallel computation, 5.39 seconds with CV-sSGLMM versus 42.2 seconds for the CV-nonSpatial. In other words, we obtain results as good or better than current state-of-the-art, but are able to do so 87% faster.

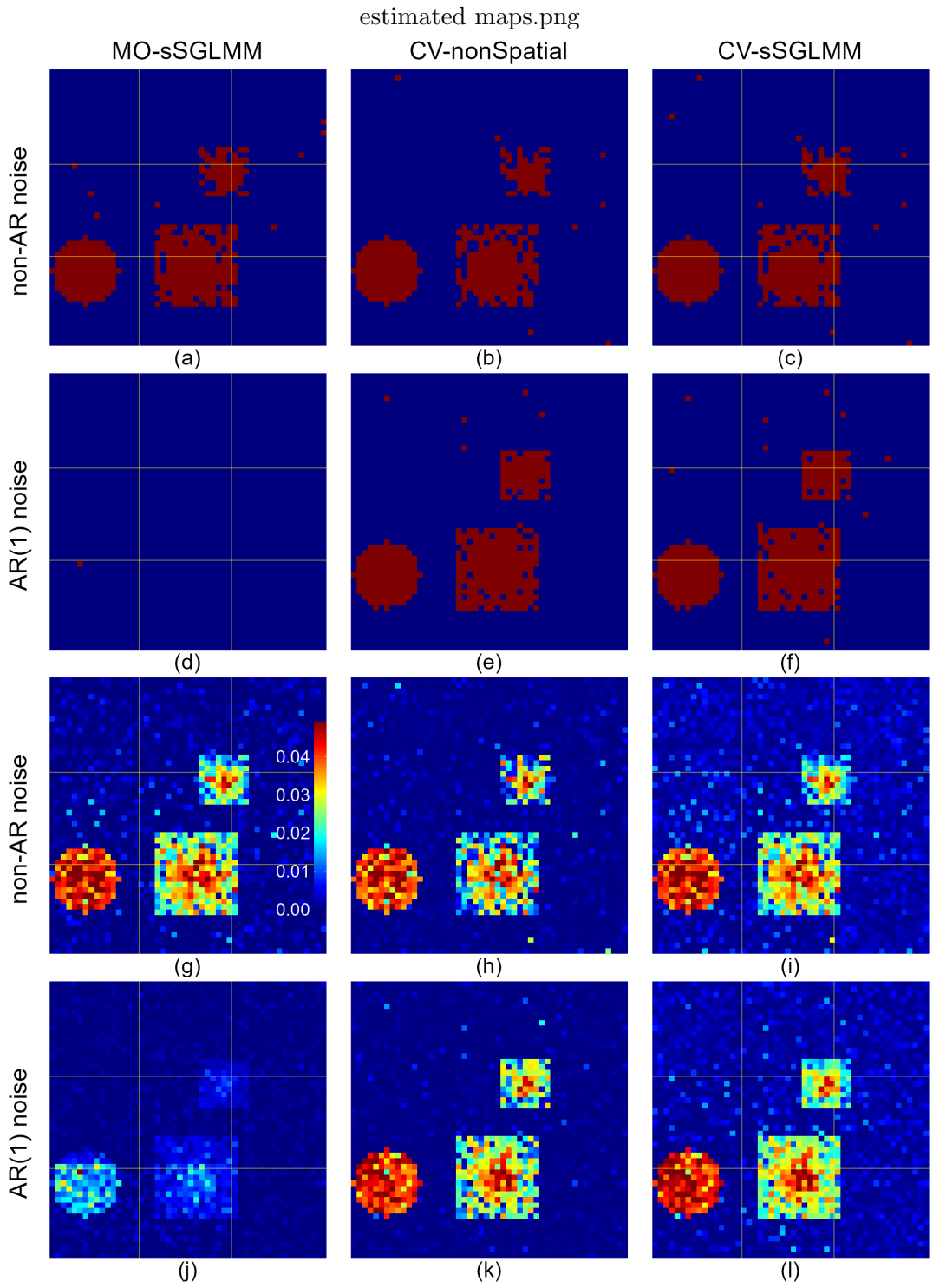

Figure 2. (a)-(c) are estimated activation maps for a non-AR dataset as produced by the MO-sSGLMM, CV-nonSpatial, and CV-sSGLMM models, respectively. (d)-(f) are estimated activation maps for an AR(1) dataset, as derived from the same models. (g)-(l) are the corresponding estimated magnitude maps.

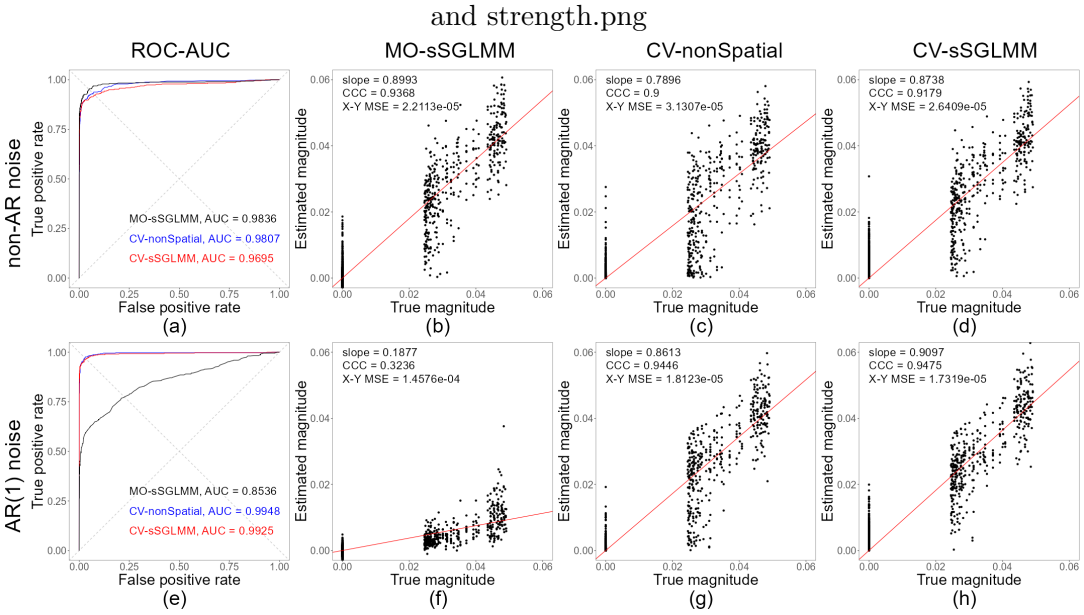

Figure 3. (a)-(d) are the ROC curves and plots comparing true versus estimated magnitudes for a non-AR dataset. (e)-(h) are analogous plots for an AR(1) dataset.

Table 2. Summary of average metrics across 100 non-AR and 100 AR(1) datasets produced by the MO-sSGLMM, CV-nonSpatial, and CV-sSGLMM models.

AR type	Mode	Accuracy	Precision	Recall	F1 Score	AUC	Slope	CCC	X-Y MSE	Time (s)
non-AR	MO-sSGLMM	**0.9693**	0.9440	**0.8160**	**0.8741**	**0.9774**	**0.8586**	**0.9008**	**2.06e-5**	**2.4**
	CV-nonSpatial	0.9540	**0.9632**	0.6687	0.7853	0.9751	0.6771	0.8222	3.04e-5	41.9
	CV-sSGLMM	0.9622	0.9277	0.7742	0.8424	0.9625	0.8186	0.8627	2.54e-5	5.51
AR(1)	CV-nonSpatial	0.9765	**0.9733**	0.8407	0.9012	**0.9927**	0.8040	0.9096	1.69e-5	42.2
	CV-sSGLMM	**0.9797**	0.9381	**0.9039**	**0.9201**	0.9879	**0.8816**	**0.9145**	**1.60e-5**	**5.39**

4. Analysis of human CV-fMRI data

In this study, we consider the fMRI dataset that is analyzed by [43], which is acquired during a unilateral finger-tapping experiment on a 3.0-T General Electric Signa LX MRI scanner. The experimental paradigm involves 16 epochs of alternating 15s on and 15s off periods, leading to $T = 490$ time points, including a warm-up period. The data are sourced from seven slices, each of size 96×96. For the MO-sSGLMM and CV-sSGLMM models, we set the parcel number to $G = 25$ and again use a threshold of 0.8722 on the inclusion probabilities. The tuning parameter ψ is set to $\Phi^{-1}(0.02)$ and $\Phi^{-1}(0.1)$, respectively. For CV-nonSpatial, the threshold is set to 0.5 as before.

The consequent activation and magnitude maps generated from these analyses are depicted in Figure 4 and Figure 5. The computation times of MO-sSGLMM, CV-nonSpatial, and CV-sSGLMM are 10.96, 305.13, and 26.45 seconds, respectively. Considering the parallel computation is gated by a 16-core CPU, the advantage becomes even more pronounced when handling larger datasets. Our CV-sSGLMM consistently demonstrates superior prediction power, particularly evident in the weakly active areas observed in slices 1 and 7. The active regions identified through our CV-sSGLMM method align with those reported in [43], reinforcing the validity of our results and the efficacy of our proposed approach. More importantly, the active regions correspond to areas of the brain that are known to typically be engaged in finger-tapping tasks, affirming the biological relevance of our findings.

5. Conclusion

In this study, we propose an innovative fully Bayesian approach to brain activity mapping using complex-valued fMRI data. The proposed model, which incorporates both the real and imaginary components of the fMRI data, provides a holistic perspective on brain activity mapping, overcoming the limitations of the conventional magnitude-only analysis methods. This model showcases the potential to detect task-related activation with higher accuracy. The adoption of an autoregressive error structure, together with spatial priors, allows us to capture both temporal and spatial correlations in brain activity. Moreover, the employment of brain parcellation and parallel computation significantly enhances the model's computational efficiency. Analyses of both simulated and real fMRI data underscores the benefits of our approach, particularly when temporally-correlated, complex-valued noise is present.

There are still areas for exploration. For instance, while we achieve significant results by assuming the phases are constant, we believe that future Bayesian studies based on the dynamic phase model of [31] should be proposed to account for potential phase variations during brain activity [24]. Additionally, our current proposal assumes circular data, that is, $\mathbf{C}^v = \mathbf{0}$ for $\boldsymbol{\varepsilon}^v$ in model (1), implying that β^v_{Re} and β^v_{Im} are independent. It would be prudent to develop a more generalized non-circular model where $\mathbf{C}^v \neq \mathbf{0}$ to account for the possibility of non-circular data.

Funding

This research is supported by the National Institute of General Medical Sciences of the National Institutes of Health under award number P20GM139769 (X. Li), and National Science Foundation awards DMS-2210658 (X. Li) and DMS-2210686 (D. A.

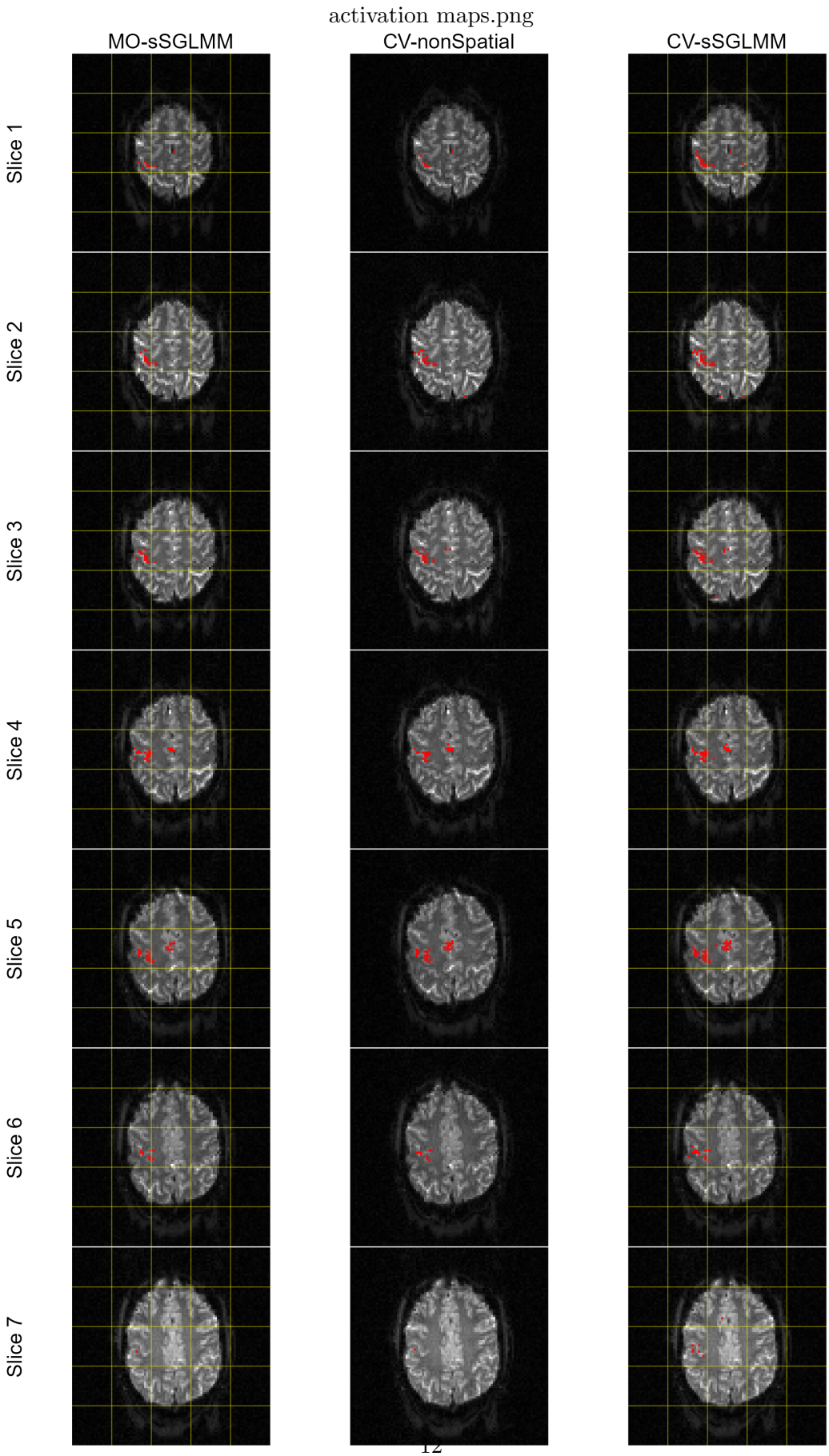

Figure 4. Estimated activation maps for a real human brain dataset as produced by the MO-sSGLMM, CV-nonSpatial, and CV-sSGLMM models

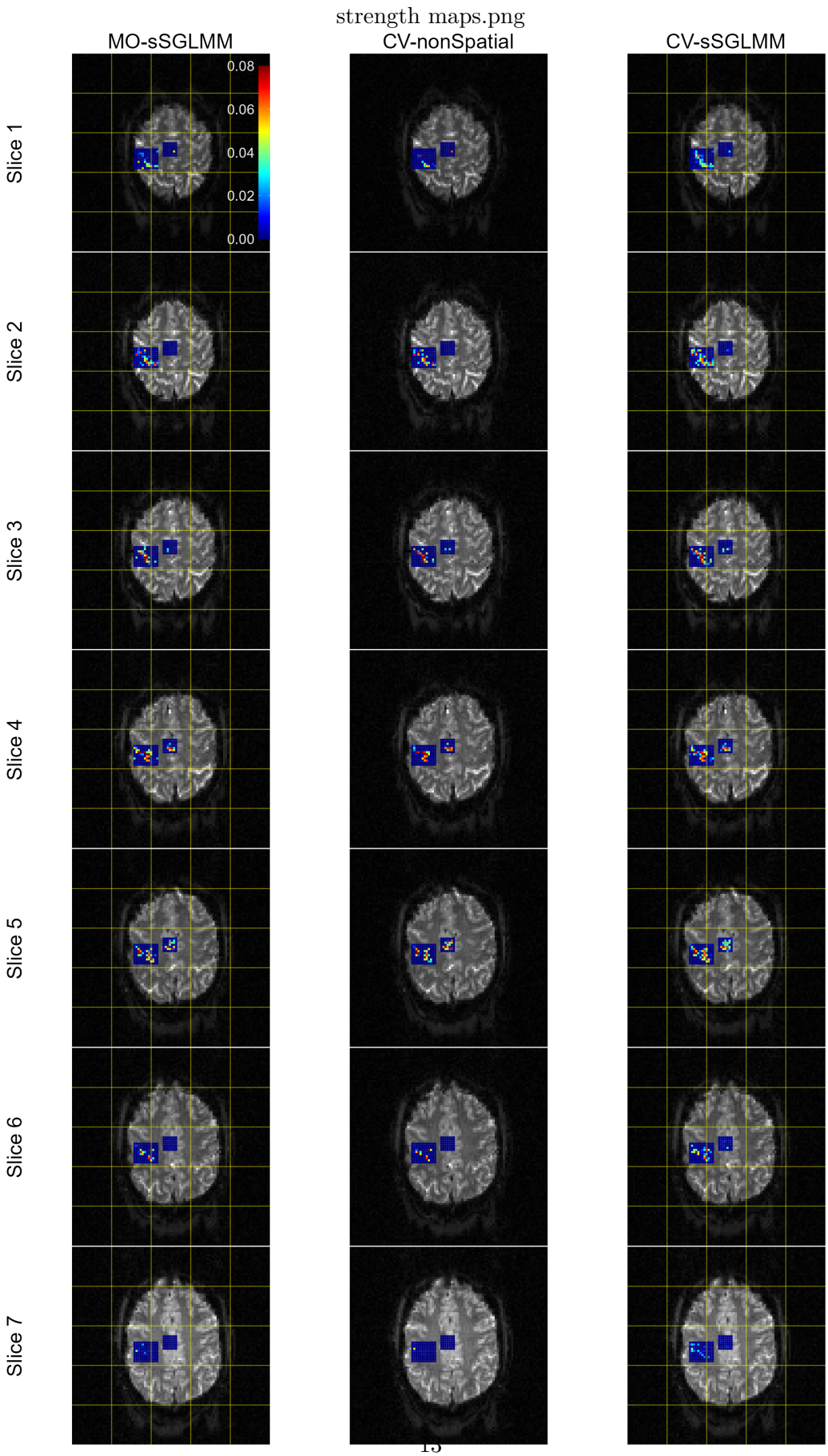

Figure 5. Estimated magnitude maps for a real human brain dataset as produced by the MO-sSGLMM, CV-nonSpatial, and CV-sSGLMM models

Brown). The content is solely the responsibility of the authors and does not necessarily represent the official views of the National Institutes of Health or the National Science Foundation.

References

[1] D.W. Adrian, R. Maitra, and D.B. Rowe, *Complex-valued time series modeling for improved activation detection in fMRI studies*, Annals of Applied Statistics 12 (2018), pp. 1451–1478. 2

[2] K. Amunts, A. Malikovic, H. Mohlberg, T. Schormann, and K. Zilles, *Brodmann's areas 17 and 18 brought into stereotaxic space – where and how variable?*, NeuroImage 11 (2000), pp. 66–84. 4

[3] P.A. Bandettini, E.C. Wong, R.S. Hinks, R.S. Tikofsky, and J.S. Hyde, *Time course EPI of human brain function during task activation*, Magnetic Resonance in Medicine 25 (1992), pp. 390–397. 1

[4] M. Bezener, J. Hughes, and G. Jones, *Bayesian spatiotemporal modeling using hierarchical spatial priors, with applications to functional magnetic resonance imaging (with discussion)*, Bayesian Analysis 13 (2018), p. 1261–1313. 2

[5] M. Bianciardi, M. Fukunaga, P. van Gelderen, S.G. Horovitz, J.A. de Zwart, K. Shmueli, and J.H. Duyn, *Sources of fMRI signal fluctuations in the human brain at rest: a 7T study*, Magnetic Resonance Imaging 27 (2009), pp. 1019–1029. 4

[6] G.M. Boynton, S.A. Engel, G.H. Glover, and D.J. Heeger, *Linear systems analysis of functional magnetic resonance imaging in human V1*, Journal of Neuroscience 16 (1996), p. 4207–4221. 1

[7] R.W. Brown, Y.C.N. Cheng, E.M. Haacke, M.R. Thompson, and R. Venkatesan, *Magnetic Resonance Imaging: Physical Principles and Sequence Design*, 2nd ed., John Wiley & Sons, Inc., Hoboken, New Jersey, 2014. 2

[8] R.W. Cox, *3dREMLfit: AFNI's New Approach to Dealing with Serial Correlation in fMRI Linear Regression (GLM)*, Presentation slides (2008). Available at https://afni.nimh.nih.gov/pub/dist/doc/misc/3dREMLfit/3dREMLfit.pdf. 3

[9] R. Epstein and N. Kanwisher, *A cortical representation of the local visual environment*, Nature 392 (1998), pp. 598–601. 5

[10] J.M. Flegal, M. Haran, and G.L. Jones, *Markov Chain Monte Carlo: Can we trust the third significant figure?*, Statistical Science 23 (2008), pp. 250–260. 6

[11] K.J. Friston, J. Ashburner, C.D. Frith, J.B. Poline, J.D. Heather, and R.S.J. Frackowiak, *Spatial registration and normalization of images*, Human Brain Mapping 3 (1995), pp. 165–189. 4

[12] K.J. Friston, A.P. Holmes, K.J. Worsley, J.P. Poline, C.D. Frith, and R.S.J. Frackowiak, *Statistical parametric maps in functional imaging: A general linear approach*, Human Brain Mapping 2 (1994), pp. 189–210. 2, 5

[13] A.E. Gelfand and A.F.M. Smith, *Sampling-based approaches to calculating marginal densities*, Journal of the American Statistical Association 85 (1990), pp. 398–409. 2

[14] H. Gudbjartsson and S. Patz, *The Rician distribution of noisy MRI data*, Magnetic Resonance in Medicine 34 (1995), p. 910–914. 2

[15] J. Hughes and M. Haran, *Dimension reduction and alleviation of confounding for spatial generalized linear mixed models*, Journal of the Royal Statistical Society. Series B (Statistical Methodology) 75 (2013), pp. 139–159. 5

[16] G. Krüger and G.H. Glover, *Physiological noise in oxygenation-sensitive magnetic resonance imaging*, Magnetic Resonance in Medicine 46 (2001), pp. 631–637. 4

[17] N.A. Lazar, *The Statistical Analysis of Functional MRI Data*, Springer, New York, 2008. 3

[18] J. Lee, M. Shahram, A. Schwartzman, and J.M. Pauly, *Complex data analysis in high-*

resolution SSFP fMRI, Magnetic Resonance in Medicine 57 (2007), p. 905–917. 2, 3

[19] M.A. Lindquist, *The statistical analysis of fMRI data*, Statistical Science 23 (2008), p. 439–464. 1, 2

[20] M.A. Lindquist, J.M. Loh, L.Y. Atlas, and T.D. Wager, *Modeling the hemodynamic response function in fMRI: efficiency, bias and mis-modeling*, NeuroImage 45 (2009), p. S187–S198. 1

[21] M. Mikl, R. Mareček, P. Hluštík, M. Pavlicová, A. Drastich, P. Chlebus, M. Brázdil, and P. Krupa, *Effects of spatial smoothing on fMRI group inferences*, Magnetic Resonance Imaging 26 (2008), pp. 490–503. 4

[22] T.J. Mitchell and J.J. Beauchamp, *Bayesian variable selection in linear regression*, Journal of the American Statistical Association 83 (1988), pp. 1023–1032. 4

[23] D.R. Musgrove, J. Hughes, and L.E. Eberly, *Fast, fully Bayesian spatiotemporal inference for fMRI data*, Biostatistics 17 (2016), pp. 291–303. 2, 4, 5, 6

[24] N. Petridou, M. Italiaander, B.L. van de Bank, J.C.W. Siero, P.R. Luijten, and D.W.J. Klomp, *Pushing the limits of high-resolution functional MRI using a simple high-density multi-element coil design*, NMR in Biomedicine 26 (2013), pp. 65–73. 11

[25] B. Picinbono, *Second-order complex random vectors and normal distributions*, IEEE Transactions on Signal Processing 44 (1996), pp. 2637–2640. 3

[26] R.A. Poldrack, J.A. Mumford, and T.E. Nichols, *Handbook of Functional MRI Data Analysis*, Cambridge University Press, New York, 2011. 3

[27] R Core Team, *R: A Language and Environment for Statistical Computing*, R Foundation for Statistical Computing, Vienna, Austria (2023). Available at https://www.R-project.org/. 7

[28] S.M. Rao, P.A. Bandettini, J.R. Binder, J.A. Bobholz, T.A. Hammeke, E.A. Stein, and J.S. Hyde, *Relationship between finger movement rate and functional magnetic resonance signal change in human primary motor cortex*, Journal of Cerebral Blood Flow and Metabolism 16 (1996), pp. 1250–1254. 5

[29] B.J. Reich, J.S. Hodges, and V. Zadnik, *Effects of residual smoothing on the posterior of the fixed effects in disease-mapping models*, Biometrics 62 (2006), pp. 1197–1206. 5

[30] S.O. Rice, *Mathematical analysis of random noise*, The Bell System Technical Journal 23 (1944), pp. 282–332. 2

[31] D.B. Rowe, *Modeling both the magnitude and phase of complex-valued fMRI data*, NeuroImage 25 (2005), pp. 1310–1324. 2, 11

[32] D.B. Rowe, *Parameter estimation in the magnitude-only and complex-valued fMRI data models*, NeuroImage 25 (2005), pp. 1124–1132.

[33] D.B. Rowe, *Magnitude and phase signal detection in complex-valued fMRI data*, Magnetic Resonance in Medicine 62 (2009), p. 1356–1360. 2, 3

[34] D.B. Rowe, A.D. Hahn, and A.S. Nencka, *Functional magnetic resonance imaging brain activation directly from k-space*, Magnetic Resonance Imaging 27 (2009), pp. 1370–1381. 4

[35] D.B. Rowe and B.R. Logan, *A complex way to compute fMRI activation*, NeuroImage 23 (2004), pp. 1078–1092. 2, 3

[36] D.B. Rowe and B.R. Logan, *Complex fMRI analysis with unrestricted phase is equivalent to a magnitude-only model*, NeuroImage 24 (2005), pp. 603–606.

[37] D.B. Rowe, C.P. Meller, and R.G. Hoffmann, *Characterizing phase-only fMRI data with an angular regression model*, Journal of Neuroscience Methods 161 (2007), p. 331–341. 2

[38] H. Rue and L. Held, *Gaussian Markov Random Fields*, Chapman & Hall/CRC, Boca Raton, 2005. 2

[39] M. Smith and L. Fahrmeir, *Spatial Bayesian variable selection with application to functional magnetic resonance imaging*, Journal of the American Statistical Association 102 (2007), pp. 417–431. 2, 5, 6

[40] N. Tzourio-Mazoyer, B. Landeau, D. Papathanassiou, F. Crivello, O. Etard, N. Delcroix, B. Mazoyer, and M. Joliot, *Automated anatomical labeling of activations in SPM using a macroscopic anatomical parcellation of the MNI MRI single-subject brain*, NeuroImage

15 (2002), pp. 273–289. 4

[41] M. Welvaert, J. Durnez, B. Moerkerke, G. Berdoolaege, and Y. Rosseel, *neuRosim: An R package for generating fMRI data*, Journal of Statistical Software 44 (2011), p. 1–18. 7

[42] M.W. Woolrich, M. Jenkinson, J.M. Brady, and S.M. Smith, *Fully Bayesian spatio-temporal modeling of fMRI data*, IEEE Transactions on Medical Imaging 23 (2004), pp. 213–231. 2

[43] C.H. Yu, R. Prado, H. Ombao, and D.B. Rowe, *A Bayesian variable selection approach yields improved detection of brain activation from complex-valued fMRI*, Journal of the American Statistical Association 113 (2018), pp. 1395–1410. 2, 3, 4, 6, 11

[44] C.H. Yu, R. Prado, H. Ombao, and D.B. Rowe, *Bayesian spatiotemporal modeling on complex-valued fMRI signals via kernel convolutions*, Biometrics 79 (2023), pp. 616–628. 2, 8